Plasma Physics and
Controlled Fusion

PAPER • OPEN ACCESS

Study of runaway electron dynamics in FTU using synchrotron spectra and imaging measurements

To cite this article: G Ghillardi *et al* 2025 *Plasma Phys. Control. Fusion* **67** 055029

OPEN ACCESS
IOP Publishing
Plasma Physics and Controlled Fusion
Plasma Phys. Control. Fusion **67** (2025) 055029 (14pp)
https://doi.org/10.1088/1361-6587/adcd9b

Study of runaway electron dynamics in FTU using synchrotron spectra and imaging measurements

G Ghillardi[1], C Barcellona[2], B Esposito[1,*], M Hoppe[3], G Pucella[1], J R Martín-Solís[4], C Monti[1], V Piergotti[1], G Rocchi[1], L Boncagni[1], F Causa[5], the FTU Team[6] and the EUROfusion Tokamak Exploitation Team[7]

[1] Dipartimento Nucleare, ENEA, C.R. Frascati, Via E. Fermi 45, Frascati, I-00044 Roma, Italy
[2] Dipartimento di Ingegneria Elettrica Elettronica e Informatica, University of Catania, 95125 Catania, Italy
[3] Department of Electrical Engineering, KTH Royal Institute of Technology, SE-11428 Stockholm, Sweden
[4] Universidad Carlos III de Madrid, Avenida de la Universidad 30, 28911 Madrid, Spain
[5] Istituto per la Scienza e Tecnologia dei Plasmi, Consiglio Nazionale delle Ricerche, ISTP-CNR, via R. Cozzi, 53, I-20125 Milano, Italy

E-mail: basilio.esposito@enea.it

Received 6 February 2025, revised 31 March 2025
Accepted for publication 16 April 2025
Published 30 April 2025

Abstract
The behavior of runaway electrons of Frascati Tokamak Upgrade (FTU) discharges is investigated through the comparison of experimental synchrotron emission spectra and visible images with their synthetic counterparts. Synchrotron spectra are measured in an unprecedented wide wavelength range (450–4000 nm) while synchrotron images are collected by a visible CCD camera. The simulated spectra and images are calculated with the synthetic synchrotron radiation diagnostic SOFT (Synchrotron-detecting Orbit Following Toolkit) code. The aim of this work is to extend the study of runaway electrons dynamics in FTU also to post-disruption phases. The runaway number, radial profile, energy and pitch angle have been evaluated during their whole time evolution, from the start-up to the post-disruption phase, assuming a given runaway electrons (RE) distribution function. The runaway number is found to increase by two orders of magnitude after the disruption, while the energy and pitch angle maintain similar values before and after the disruption. The runaway electrons are mostly distributed in the core

[6] See Pucella *et al* 2019 (https://doi.org/10.1088/1741-4326/ab19ef) for the FTU Team.
[7] See Joffrin *et al* 2024 (https://doi.org/10.1088/1741-4326/ad2be4) for the EUROfusion Tokamak Exploitation Team.
[*] Author to whom any correspondence should be addressed.

of the plasma. The inferred maximum RE energy and pitch angle are in agreement with the results of simulations based on a runaway electron test particle model.

Keywords: runaway electrons, synchrotron radiation, Tokamak

1. Introduction

One of the main challenges for future fusion devices is the identification and control of runaway electrons (RE). In present fusion machines, sufficiently strong electric fields can accelerate electrons to relativistic speeds, overcoming the collisional friction. This situation can occur in different discharge phases, during the plasma current (I_p) ramp-up, during the I_p flat-top if the electron density is low or in the plasma disruption when the magnetic confinement and the thermal energy are decreasing. RE created in this latter process can potentially damage plasma-facing components. Several experiments reported damages caused by RE and this is a matter of serious concern for all large tokamaks, such as ITER [1]. Disruption mitigation systems are envisioned for ITER, and they mainly rely on impurity injection into the plasma with the goal of radiating away most of the stored energy without any structural damage [2].

Studies of RE dynamics in the Frascati Tokamak Upgrade (FTU) were carried out as early as 2003 during the I_p ramp-up and flat-top of ohmic discharges [3]. The dynamics of RE was investigated using a gamma-ray spectrometer, measuring the gamma-ray spectra produced by thick-target bremsstrahlung of RE, and a fast electron bremsstrahlung (FEB) monitor. The gamma-ray system was used for the analysis of the RE energy evolution while the FEB system provided information on the generation, location and confinement of the runaway population. The RE were found to be generated in the central region of the plasma early in the discharge. The runaway production can be explained by the Dreicer (primary) mechanism, although the additional presence of the avalanche (secondary) mechanism cannot be ruled out. The generation process takes place during the I_p ramp-up, when the electron density is low and the electric field is high. The generated RE can be detected for more than one second, during the whole discharge time. The RE population tends to form a monoenergetic electron beam [3] with an energy equal to the limiting energy resulting from the balance between the energy gain in the electric field and the energy losses due to plasma collisions and synchrotron radiation [4]. Maximum energy values in the range 5–35 MeV were inferred [3].

Lately, a more extensive suite of RE diagnostics was used [5, 6] to investigate the processes of RE generation and suppression in FTU RE stationary discharges, basically confirming earlier results: maximum energy values in the range 5–35 MeV and pitch angles of the order of 0.1 rad were inferred through synchrotron radiation (imaging and spectrometry), while the details on the local RE losses linked to MHD activity were provided by a Cherenkov probe [7]. Moreover, measurements of the upper and lower bounds of the threshold electric field for RE generation (E_{thr}) were obtained indicating that E_{thr}, while being larger by a factor 2–5 than expected according to the purely collisional theory, reasonably agrees with the new threshold calculated including synchrotron radiation losses [8]. In addition, in [6] a characteristic runaway dissipation time τ_d was found in the range 0.05–0.3 s. This can be attributed to radial diffusion losses (as observed in [3]) such as those driven by the underlying magnetic turbulence, but the presence also of other mechanisms (e.g. kinetic instabilities) cannot be ruled out.

The aim of this work is to extend the study of RE dynamics in FTU also to post-disruption phases. We will follow the RE evolution from the I_p start-up phase up to the post-disruption runaway beam phase. The FTU discharges that were analyzed are part of a set of recent experiments carried out in order to investigate the RE mitigation strategies for quiescent and post-disruption RE beams [9]. Pellet injection into discharges with RE seeding led to disruption and subsequent RE beam formation.

RE synchrotron images collected in the visible range (400–650 nm) and spectral measurements performed in an unprecedentedly wide wavelength range (450–4000 nm) were used for this study. Measurements of synchrotron radiation emitted by runaway electrons are widespread in tokamaks. The pioneering studies were carried out in TEXTOR by means of infrared (IR) cameras [10, 11]. Later on imaging cameras were employed in several tokamaks: (a) during the I_p flattop using an IR camera (7500–13 000 nm) in HT-7 [12], a visible camera (380–750 nm) [13] and an IR camera (3000–4900 nm) [14] in EAST, an IR camera (3000–5000 nm) in KSTAR [15], a visible camera (400–900 nm) in Alcator C-Mod [16], a visible camera equipped with a narrow band centered at 890 nm in DIII-D [17], a visible camera detecting radiation in a narrowband filter centered at 640.6 nm [18] and a multispectral imaging camera (640.6 nm, 800 nm, 950 nm) [19] in TCV; (b) during the post-disruption phase using an IR camera (3000–3500 nm) in JET [20] and a visible camera equipped with a narrow band near 709 nm in AUG [21]. Spectrometers were used as well in previous work, but less frequently: in the (400–850 nm) range in DIII-D [22], in the (300–1000 nm) range in Alcator C-Mod [23] and in the (370–2100 nm) range in FTU [5, 24].

In this work for the first time the combination of synchrotron images and spectra is used in order to infer parameters of the RE distribution function. Synchrotron radiation, emitted by relativistic electrons as a consequence of their gyro motion, depends on their energy, pitch angle, number and radial distribution in the vessel. Such parameters are inferred for the RE population by assuming a given RE distribution function decoupled in functions of the momentum, pitch angle and radial coordinate. The analysis method is based on the comparison of the experimental synchrotron radiation spectra and images with their simulated counterparts calculated using the Synchrotron-detecting Orbit Following Toolkit (SOFT) code. SOFT [17] is a synthetic diagnostic framework capable of computing the synchrotron image and spectrum generated by a population of relativistic electrons by solving the guiding-center equations of motion, taking into account the spatial position and the field of view (FOV) of the synchrotron diagnostics. The distribution function of the relativistic electrons is not calculated by the code, but is given as an input in a pre-set form chosen by the user, that is checked *a posteriori* for consistency with the experimental data.

The observations are described in section 2, the experimental set-up of the synchrotron diagnostics is presented in section 3, the analysis method using SOFT is described in section 4 and the determination of the RE distribution function parameters is provided in section 5. The discussion on the RE dynamics, especially in the post-disruption phase, is provided in section 6 and the conclusions are given in section 7. The procedure of the spectral measurements calibration is reported in appendix.

2. Observations

The two discharges analyzed in the paper were carried out in FTU (major radius $R = 0.935$ m, minor radius $r = 0.3$ m, toroidal magnetic field $B_t = 2$–8 T, $I_p = 0.2$–1.6 MA) during RE experiments performed in September 2019 with different B_t and I_p values: #43651 ($B_t = 5.3$ T, $I_p = 0.35$ MA) and #43540 ($B_t = 6$ T, $I_p = 0.5$ MA). These pulses have a significant RE seeding population, i.e.: quiescent RE scenarios, in which D_2 pellet injection has been performed in order to investigate the RE mitigation capabilities in support of ITER safe operation [9]. Such scenarios were achieved by using a low D_2 gas prefill and reducing the electron density (n_e) reference below 3×10^{19} m^{-3}. The time traces of the two discharges are reported in figure 1. In discharge #43651 I_p, after a ramp-up phase, reaches the flat-top where a disruption is induced by means of deuterium pellet injection. A first D_2 pellet injection is at 0.300 s (2x10^{20} atoms) and a second D_2 pellet injection occurs at 0.378 s (1x10^{20} atoms). After the first pellet cools the plasma, the control loop reacts to the I_p, that slowly decreases due the increased resistivity, by increasing the current rate on the ohmic transformer, and consequently, slowly increasing the electric field (measured by the loop voltage (V_{loop})). This electric field accelerates further the RE; a further acceleration of the pre-existing RE occurs at the following disruption. Mild MHD activity is seen just before the I_p quench. Discharge #43540 is similar, but I_p does not reach a flat top; the RE beam is formed after the injection of D_2 pellets at 0.284 s (2 small pellets, 1x10^{20} atoms each, and 1 large pellet, 2x10^{20} atoms, injected simultaneously) and lasts for more than 0.4 s.

In the pre-disruption phase both plasmas have a high effective ion charge (Z_{eff} in the range 7–10), that subsequently decreases (Z_{eff} in the range 2–4). Note that FTU has a stainless steel vacuum chamber covered internally, on the high field side (HFS), by a toroidal limiter made of molybdenum tiles; a molybdenum poloidal limiter is also present on the low field side (LFS) [25]. The high Z_{eff} values in the pre-disruption phase is typical of low density discharges [5]. RE are generated in both discharges during the I_p ramp-up phase as shown by the hard-x rays (measured by a NE213 scintillator) and the synchrotron radiation (measured by the integrated spectral signals of three spectrometers operating in different spectral ranges (see next section)). When the disruption is induced, there is an immediate strong increase of the bremsstrahlung gamma radiation (indeed the NE213 scintillator signal saturates) and of the synchrotron radiation (see bottom panels in figure 1) which peaks 30 ms after the pellet injection. The neutron signal (^{235}U fission chambers [26], third panel from the top in figure 1) also increases after the disruption (peaking almost simultaneously with the synchrotron radiation) indicating the presence of RE with energy in excess of 7 MeV producing hard x-rays by target bremsstrahlung on the vessel structures and, therefore, neutrons by photodisintegration. Note that the synchrotron and neutron signals share the same time behaviour, decreasing, after the initial peak, throughout the RE beam phase.

3. Experimental set-up

An enhanced spectrometer system belonging to the runaway electron imaging and spectroscopy system diagnostic (REIS) [24] was used in conjunction with a fast CCD visible camera [27]. Figure 2 shows the layout of the spectrometers and the CCD camera in the FTU tokamak. The camera and spectrometer FOV are shaded, respectively, in grey and brown. The spectrometer system is composed of four spectrometers (figure 3): each spectrometer has either a RE forward (FW) or backward (BW) direction, while the camera is viewing simultaneously the FW and BW directions. The parameters of the spectrometers and of the camera are summarized in table 1, following the notation in [17]. Examples of the experimental CCD images and spectra acquired in FTU in RE experiments are shown in figures 4 and 5, respectively.

Three spectrometers are for RE FW view: an Ocean Optics model HR2000+ for the VIS range (374–826 nm), an Ocean Optics model NIRQuest for the NIR range (878–2500 nm) and a SpectralProducts Model SM301 for the MIR range (1430–5030 nm). The overall effective range of the FW view spectrometer system is limited to the range 450–4000 nm once the calibration procedure is applied (see appendix). One VIS spectrometer is used to monitor/cross check the RE BW view: it is of the same type as the other VIS spectrometer used for the FW view. The synchrotron radiation is collected by a wide-angle CaF2 lens and routed to the spectrometers through an incoherent 19 m long bundle of optical fibers. The lens and the fibers, as shown in figure 3, are inserted in a protective tube with a BK7 glass window. The BK7 has a transmission gap

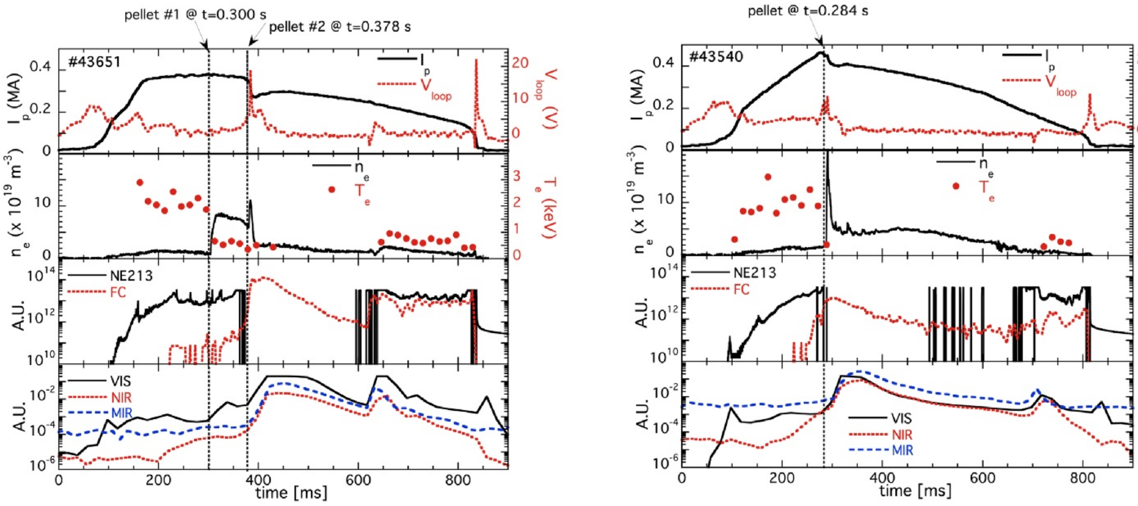

Figure 1. Discharges #43651 (left) and #43540 (right). From top to bottom: I_p and V_{loop}, central line-averaged electron density (from CO_2 interferometer) and central temperature (from Thomson scattering), gamma-ray/neutron signals, integrated synchrotron spectra in visible (VIS), near InfraRed (NIR) and medium IR (MIR) ranges.

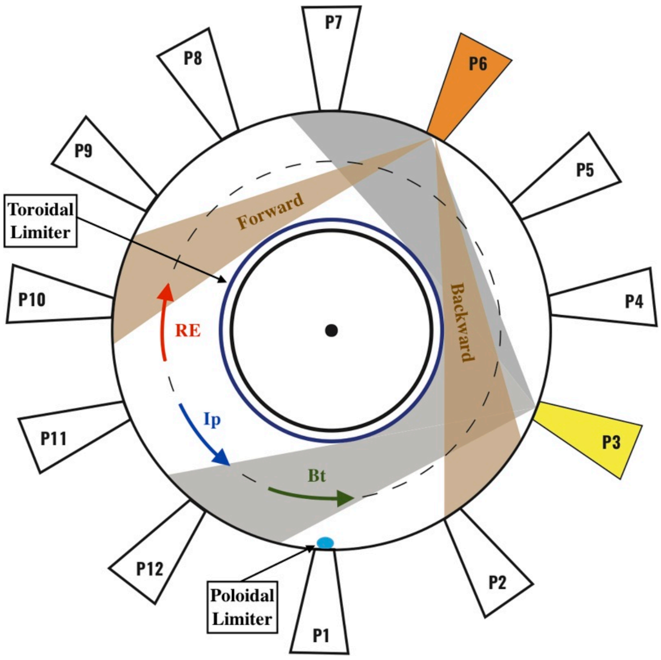

Figure 2. Schematic view of the FTU mid-plane cross section, showing the location of the spectrometers' head in port 6 (P6) and CCD camera in port 3 (P3).

around 2700 nm that is corrected in the spectrum calibration. The optical head connected to the spectrometers was installed in port 6 on the equatorial plane at $z = 0$ cm and at a distance of approximately 35 cm from the vacuum vessel axis. The spectra are calibrated and cleared of saturated wavelengths. The acquisition software [3] is written in LabVIEW^{TM} and is based on the FTU discharge phases PRE-RUN, START-RUN, END-RUN. The VIS and NIR spectra were acquired every 20 ms while the integration time window was set at 15 ms. The MIR spectrometer acquired data every 15 ms with an integration window of 15 ms.

The fast CCD camera (Toshiba model IK-M51H, sensitive in the visible range) was installed in port 3 at $z = -0.105$ m and at a distance of 35 cm from the vacuum vessel axis. This camera captures images every 40 ms with a FOV of 111°. The images were spatially calibrated using the OpenCV library [28] and chess board images taken in the laboratory after the experimental campaign. The RE signal in the discharges produced experimental visible images reaching over 80% of the camera dynamics. For the analysis carried out in the following sections, a filtering process is applied to the images by setting to zero all the pixels which are fainter than 70% of the maximum intensity, in order to remove light due to reflections and isolate the RE synchrotron spot from the surrounding noise, see figure 6. The task of evaluating the contribution of reflections is difficult since the wall reflectivity is generally unknown. A first attempt to evaluate reflection effects in synchrotron camera images in JET has been made recently in [29].

4. Analysis method

The analysis method is based on the comparison of experimental and simulated synchrotron spectra and images. The RE synchrotron emission is simulated by SOFT [17], a synthetic synchrotron diagnostic framework based on a guiding-centre discretization of space. For our study we used three types of SOFT outputs: spectra and images to compare with experimental data, and Green's functions for performing the analysis on the RE distributions.

SOFT calculates the amount of synchrotron radiation at a given wavelength that reaches an observer at $\mathbf{x}_0$ from a population of runaway electrons, represented by a distribution

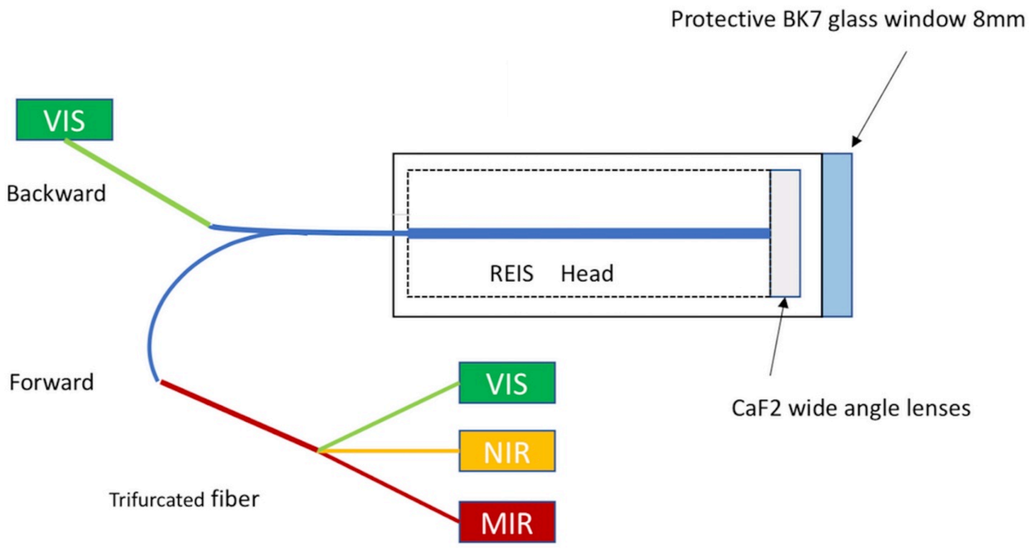

Figure 3. Schematic drawing of the spectrometer system.

Table 1. Parameters of the spectrometer system and CCD camera.

Parameter	Spectrometers	Camera
Aperture (square side length)	0.017 m	0.017 m
Position (X, Y, Z)	$[0, -1.265, 0]$ m	$[0, -1.265, -0.105]$ m
Viewing direction (n_x, n_y, n_z)	[0.5,0.87,0]	[0, 1, 0]
Field of view [FOV]	0.52 rad	1.93 rad
Spectral range	[374, 5030] nm	[400, 650] nm
Rotation angle (roll)	0 rad	0.131 rad (CW)
Acquisition rate	50 Hz (VIS, NIR) 66.7 Hz (MIR)	25 Hz

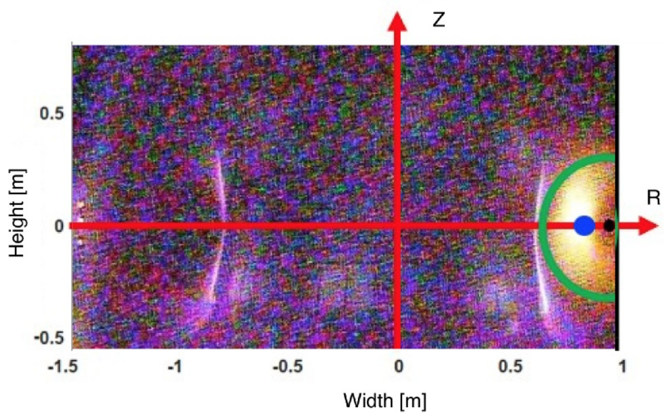

Figure 4. Experimental CCD image (discharge #43651, $t = 700$ ms): the RE synchrotron spot in the forward direction and the contour of the plasma outer boundary (represented as a green circle) are seen in right side of the picture. The inner vessel is also visible. The position of the geometrical axis (R_0) and the magnetic axis (R_{ax}) from equilibrium reconstruction are shown in black and blue, respectively.

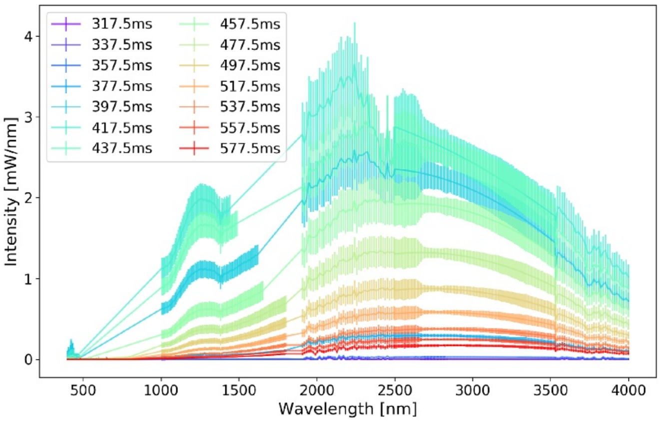

Figure 5. Experimental synchrotron spectra for forward view (discharge #43651, disruption at = 377 ms). Data are calibrated, cleared of saturated zones and interpolated. Shadowed bands represent the estimated error bars.

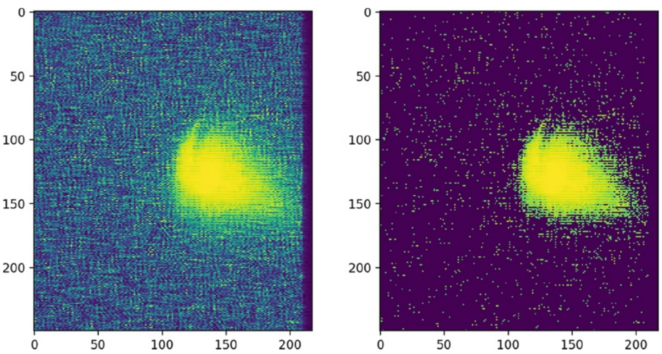

Figure 6. Example of image correction in discharge #43651 at 540 ms: on the left the full signal image, on the right the signal after the noise filter application, both in monocromatic scale.

function $f(\mathbf{x},\mathbf{p})$ for position $\mathbf{x}$ and momentum $\mathbf{p}$, in a given magnetic field:

$$\frac{\mathrm{d}I}{\mathrm{d}\lambda} = \int \Theta\left(\frac{\mathbf{x}_0-\mathbf{x}}{|\mathbf{x}_0-\mathbf{x}|}\right)\frac{(\mathbf{x}_0-\mathbf{x})\cdot\hat{\mathbf{n}}}{|\mathbf{x}_0-\mathbf{x}|^3}\frac{\mathrm{d}P}{\mathrm{d}\lambda\mathrm{d}\Omega}f(\mathbf{x},\mathbf{p})\,\mathrm{d}\mathbf{x}\,\mathrm{d}\mathbf{p}\,\mathrm{d}A. \tag{1}$$

Here, $\Theta(\mathbf{v})$ is a step function which is one if the vector $\mathbf{v}$ lies within the field-of-view of the detector, $\hat{\mathbf{n}}$ is a unit vector which is normal to the detector surface, and $\mathrm{d}P/\mathrm{d}\lambda\mathrm{d}\Omega$ is the angular and spectral distribution of radiation emitted by a single particle. The differential $\mathrm{d}A$ indicates that integration should performed across the aperture of the detector. When considering the pixels of a camera, we evaluate equation (1) separately for each pixel, and integrate the contribution from all wavelengths to which the camera is sensitive. It is important to stress that in the following analysis the distribution f is assumed given and fixed, based on parametrizations as explained in detail below. To reduce the number of dimensions in f, and improve computational speed, SOFT utilizes that according to Liouville's theorem, f must be constant along trajectories in phase-space. Therefore, instead of discretizing the integral (1) using e.g. a uniform mesh in phase-space, which would require storing the value of f in a six-dimensional space, we parametrize it using the orbit coordinates $(\mathbf{x},\mathbf{p}) = (r,\theta,\phi,p,\theta_p,\zeta)$, where r is the radial coordinate, θ is the poloidal angle, ϕ is the toroidal angle, p is total momentum (normalized to the electron rest mass $m_\mathrm{e}c$), θ_p is pitch angle and ζ is the gyro angle. Using arguments of symmetry it can be concluded that f is independent of ϕ and ζ, while, since the effects of collisions on runaway electrons are negligible on the poloidal transit time scale, we can consider that f is also independent of the poloidal angle θ [17].

For the purpose of studying the sensitivity of the synchrotron diagnostic to runaway electrons, it can be useful to separate and pre-evaluate those parts of the integral which f is independent of. Hence, the integral (1) can also be written in terms of the Green's function $\hat{I}(r,p,\theta_p)$ for the diagnostic as:

$$I = \int\int\int f(r,p,\theta_\mathrm{p})\,\hat{I}(r,p,\theta_p)\,\mathrm{d}r\mathrm{d}p\mathrm{d}\theta_p. \tag{2}$$

Apart from being useful in studying the sensitivity of the diagnostic, the Green's function $\hat{I}$ also enables us to constrain the distribution function by experimental measurements of synchrotron radiation.

$\hat{I}$ contains the radiation function of the particle, $\mathrm{d}P/\mathrm{d}\lambda\mathrm{d}\Omega$, that can be treated in many different ways; in this study we opt to use the so-called cone model, as implemented in SOFT, in which the synchrotron radiation is assumed to be emitted in a circular cone around the guiding-center velocity vector, as described in more detail in (1). Specifically, we take the angular and spectral distribution of synchrotron radiation to be:

$$\left\langle\frac{\mathrm{d}^2P}{\mathrm{d}\lambda\mathrm{d}\Omega}\right\rangle = \frac{1}{2\pi}\frac{\mathrm{d}P}{\mathrm{d}\lambda}\delta\left(\cos\mu-\cos\theta_p\right) \tag{3}$$

where angular brackets denote an average over the gyro-angle, μ is the angle between the velocity vector of the guiding-center and the observation vector $\mathbf{x}_0-\mathbf{x}$, and $\mathrm{d}P/\mathrm{d}\lambda$ is the spectral distribution of synchrotron radiation [30]:

$$\frac{\mathrm{d}P}{\mathrm{d}\lambda} = \frac{1}{\sqrt{3}}\frac{ce^2}{\epsilon_0\lambda^3\gamma^2}\int_{\lambda_\mathrm{c}/\lambda}^{\infty}K_{5/3}(l)\,\mathrm{d}l, \tag{4}$$

where e is the electron charge, c is the speed of light, ϵ_0 is the vacuum permittivity, $K_{5/3}(x)$ is the modified Bessel function of second kind and order $5/3$, γ is the relativistic factor, β is the electron speed normalized to c, λ is the wavelength, and λ_c is the critical wavelength.

The following approximations and experimental inputs are used for performing the simulations:

- approximations:
  - cone model approximation (circular cone of radiation emitted by guiding-center orbit with half opening angle θ_p, centered on its direction of motion $\mathbf{V}$);

– instead of the numerical magnetic field, whose uncertainties did not allow us to obtain stable simulation results, we opted for an analytical magnetic field. This option in SOFT allows the user to specify common properties of the magnetic field, such as its on-axis strength and major radius, and generates a magnetic field with circular flux surfaces that is a reasonable approximation in the circular tokamak FTU. The magnetic field vector (derived in the large-aspect ratio limit) is:

$$B(r,\theta) = \frac{B_0 R_\mathrm{m}}{R_\mathrm{m} - r\cos\theta}\left(\frac{r\sigma_I}{q(r)R_\mathrm{m}}\hat{\theta} + \sigma_B\hat{\varphi}\right) \quad (5)$$

where r and R_m denote the minor and major radius of the machine respectively, θ denotes the poloidal angle, $\hat{\theta}$ and $\hat{\varphi}$ are unit vectors in the poloidal and toroidal directions respectively, σ_B and σ_I the toroidal field and plasma current sign, B_0 is the on-axis magnetic field strength, and $q(r)$ is the safety factor, fitted to the experimental profile using a quadratic polynomial;

— the drift orbit shift, corresponding to the first-order terms in the guiding-center equations of motion, are neglected. In practice, this means that electrons exactly follow flux surfaces, while their pitch angles evolve due to the variation of the magnetic field strength along the flux surface.

- experimental inputs:
  - coordinates and parameters of synchrotron diagnostics (see table 1);
  - minor/major radii of the tokamak and time traces of the safety factors radial profiles (q_edge and q_axis) provided by the equilibrium reconstruction plasma parameters (see figure 7);
  - the number of toroidal section to divide the tokamak into is 7000. This is the resolution parameter for the toroidal integral in the radiation diagnostic integral;
  - time-steps, respectively 2000 for spectra and 7000 for images, indicate the number of time steps per orbit. The orbit quantities (particle position and momentum) are given in a uniformly distributed set of time points in one orbit;
  - integration time: one poloidal transit time.

The chosen distribution function of the RE is a parametrized approximation, namely:

$$f(r,p,\theta_\mathrm{p}) = f_r(r)\,\delta(p-p^*)\,\mathrm{e}^{K\cos\theta_\mathrm{p}} \quad (6)$$

that is physically justified as follows. The use of the delta function in p (i.e.: monoenergetic distribution) is justified by the results of earlier RE dynamics studies in the pre-disruption phase of similar FTU discharges, which indicated the formation of almost monoenergetic RE beams in similar plasma conditions [3, 4]. The effect of alternative energy distributions would not be major: the synchrotron spot shape depends only very weakly on the energy, and is due to the drift-orbit shift. With a distribution of energies, we would obtain a weighted sum of synchrotron spots corresponding to each

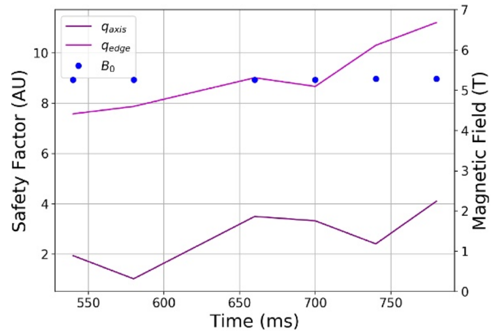

Figure 7. Safety factors and magnetic field values in discharge #43651 at times of images analysis.

energy in the distribution, with stronger contributions at higher energies. The energy distribution can just contribute to 'blurring' the spot, since spots corresponding to different energies will have a somewhat different dependence on magnetic field strength [17, 31]. The fact that the synchrotron pattern is rather insensitive to variations in the runaway energy distribution is also used to fully decouple the spatial coordinate r from the momentum parameter p and, since K is mainly a function of p, also from K. In this model we thus assume for simplicity that the momentum and pitch distributions are the same across all flux surfaces [21].

The choice of the the pitch angle distribution $\mathrm{e}^{K\cos\theta_\mathrm{p}}$ is motivated by the following reason. In the plateau phase of a disruption, the pitch distribution of the runaways will be set by a balance between the electric field (which settles on a value close to the avalanche threshold, $E = E_\mathrm{c}$ [32, 33]) and pitch angle scattering and this does not depend on how RE have been generated. The RE distribution f will therefore satisfy the following kinetic equation [34]:

$$\frac{\partial f}{\partial t} = \frac{\partial}{\partial \xi}\left[\left(1-\xi^2\right)\left(-\frac{E}{pE_\mathrm{c}}f + \frac{\nu_\mathrm{D}(p)}{2}\frac{\partial f}{\partial \xi}\right)\right], \quad (7)$$

where $\nu_\mathrm{D}(p)$ is the pitch angle deflection frequency and $\xi = \cos\theta_p$. Assuming weakly varying plasma parameters in the plateau phase, taking the steady state limit ($\partial f/\partial t \to 0$) of this equation, and integrating once with respect to ξ on the range $[-1,\xi]$, yields

$$\frac{\nu_\mathrm{D}}{2}\frac{\partial f}{\partial \xi} = \frac{E}{pE_c}f, \quad (8)$$

which is generally solved by

$$f(t,p,\xi) = F(t,p)\frac{K}{2\sinh K}\exp(K\xi), \quad (9)$$

with $K = 2E/(E_\mathrm{c}p\nu_\mathrm{D})$. We note that the energy distribution $F(t,p)$ is decoupled from the pitch distribution, which takes the simple form $f(\xi) \sim \mathrm{e}^{K\xi}$. Kinetic simulations show that even before the distribution reaches the steady state, pitch angle scattering often leads the pitch distribution to take the same exponential form displayed here. The coefficient K is however in that case not the same simple function of E and ν_D as here, but instead varies in time and approaches its steady state value as t^{-1} (see appendix B of [21]).

The pitch distribution function f in (6) is monotonically decreasing with θ_p, while the emitted synchrotron radiation intensity $\hat{I}$ is monotonically increasing. This causes the detected radiation to have the characteristics of the particles which dominate the emission, i.e. which are sufficiently numerous while at the same time emitting enough radiation at the same points in space. Mathematically we can characterize this θ_p by maximizing the integrand of equation (2), and here we will call this pitch angle corresponding to the maximum of the product $f\hat{I}$

$$\theta_K \equiv \max_{\theta_p}\left(f\hat{I}\right). \tag{10}$$

The subscript K indicates that the value of this angle directly depends on the factor K appearing in the exponent of the pitch angle distribution. Later in this paper we will associate a pitch angle with the synchrotron radiation measurements, and it is θ_K which is exactly this associated pitch angle.

The value of p^* and the dependence of f on pitch angle and r (all as a function of time) are determined through an iterative process in two steps (section 5). In the first step the purpose is only that of finding the best match between measured and simulated spectra and therefore we assume a simplified version of the distribution of equation (6) in which the pitch angle and r are kept constant. This approach is justified since the fitting of the spectra does not depend much on the type of functional dependence on the pitch angle and on the radius, but, rather, only on the value of p. In the second step also the experimental images are used in the analysis and the full distribution as indicated in (6) is employed. At the end of section 5 it will be shown a-posteriori that no good matching can be obtained between simulated and experimental images unless the correct dependence in pitch angle and radius as in (6) is used.

5. Determination of the RE distribution parameters

First, a comparison is made between measured and simulated synchrotron spectra. For each time slice, several simulations of the synchrotron spectrum are performed by varying the RE energy (namely the normalized momentum p) and pitch angle values (a suitable grid of values is used, typically in the 5–50 MeV energy range and 0.1–0.3 rad pitch angle range, using mono-energetic and mono-pitch distributions.

Since SOFT does not take into account the number of simulated electrons, the comparison between power intensities of simulated ($\mathrm{d}I_{\mathrm{simu}}/\mathrm{d}\lambda$) and experimental ($\mathrm{d}I_{\mathrm{data}}/\mathrm{d}\lambda$) spectra must take into account a multiplicative factor C, constant over the wavelengths, such that $\mathrm{d}I_{\mathrm{data}}/\mathrm{d}\lambda \approx C \times \mathrm{d}I_{\mathrm{simu}}/\mathrm{d}\lambda$. This factor is proportional to the number of runaways N_{RE}: SOFT spectra are computed from a RE distribution in the phase-space, hence, the $\mathrm{d}I_{\mathrm{simu}}/\mathrm{d}\lambda$, must be normalized for the phase-space volume selected ($V_{\mathrm{SOFT}} = \int f(r,p,\theta_p)\,\mathrm{d}r\,\mathrm{d}p\,\mathrm{d}\theta_p$), in order to represent the intensity of a single electron. The C parameter is estimated, for each time, as the value which minimizes the sum of the square error ($E(C)$) of the single wavelength power intensities ($\mathrm{d}I_{\mathrm{simu}}/\mathrm{d}\lambda$ and $\mathrm{d}I_{\mathrm{data}}/\mathrm{d}\lambda$):

$$E(C) = \sum_i \left[\frac{\mathrm{d}I_{\mathrm{data}}}{\mathrm{d}\lambda}(\lambda_i) - C\cdot\frac{\mathrm{d}I_{\mathrm{simu}}}{\mathrm{d}\lambda}(\lambda_i)\right]^2. \tag{11}$$

The mean of $E(C)$ in wavelengths is used as the mean square error in this analysis. For each time, a scan over simulations at different energy and pitch angle is performed, and the one with the lower $E(C)$ is selected.

The number of RE is computed from the C parameter as:

$$N_{\mathrm{RE}} = \frac{\mathrm{d}I_{\mathrm{data}}/\mathrm{d}\lambda}{(\mathrm{d}I_{\mathrm{simu}}/\mathrm{d}\lambda)/V_{\mathrm{SOFT}}} = C\cdot V_{\mathrm{SOFT}} \tag{12}$$

The best fit of the spectrum for each time instant provides working estimates of normalized *momentum and pitch angle* couples (different combinations of normalized *momentum and pitch angle* give similar spectra) as well as the total RE number. Note that the estimated RE number does not practically depend on the selected pitch angle and/or energy and, incidentally, note also that the approximation of mono-energetic distribution used in this paper may lead to an underestimate of the total number of runaways since the contribution of less energetic particles to the synchrotron spectra is missing.

Secondly, the experimental images and the simulated Green's functions obtained using the K values selected are used (i.e.: the p^*, K and θ_K values coupled in the previous step). In order to obtain the radial distribution that enables the best matching between experimental and simulated images, using the inversion algorithm as presented in [21], we make use of the Green's function SOFT output. This output module enables the use of many different types of Green's functions, which may be integrated over any or all of phase space, the image pixels and/or the detector spectral range.

With the use of the Green output the RE radial profile is selected, by comparing each pixel's simulated intensity with the experimental one from the CCD camera. In this step, we create unique combinations of momentum p^*, the pitch angle parameter K, and the radial profile $f_r(r)$. With such information, the simulated images are created and the combination is selected as the best fit between synthetic images and real ones. Note that this step can be performed only at times when synchrotron images are available.

In summary, firstly, we have determined the RE number and (p^*,K) couples, and secondly, we have added the radial info to each (p^*,K) couple and determined the best parameters of the assumed distribution function. The results of these processes are summarized, respectively, in figure 8 (showing four subsequent time slices of the simulated and experimental spectra in discharge #43651) and in figure 9 (showing for the same discharge the time sequence of the simulated and experimental images). Figure 10 shows the RE radial profiles in the same time slices as in figure 9.

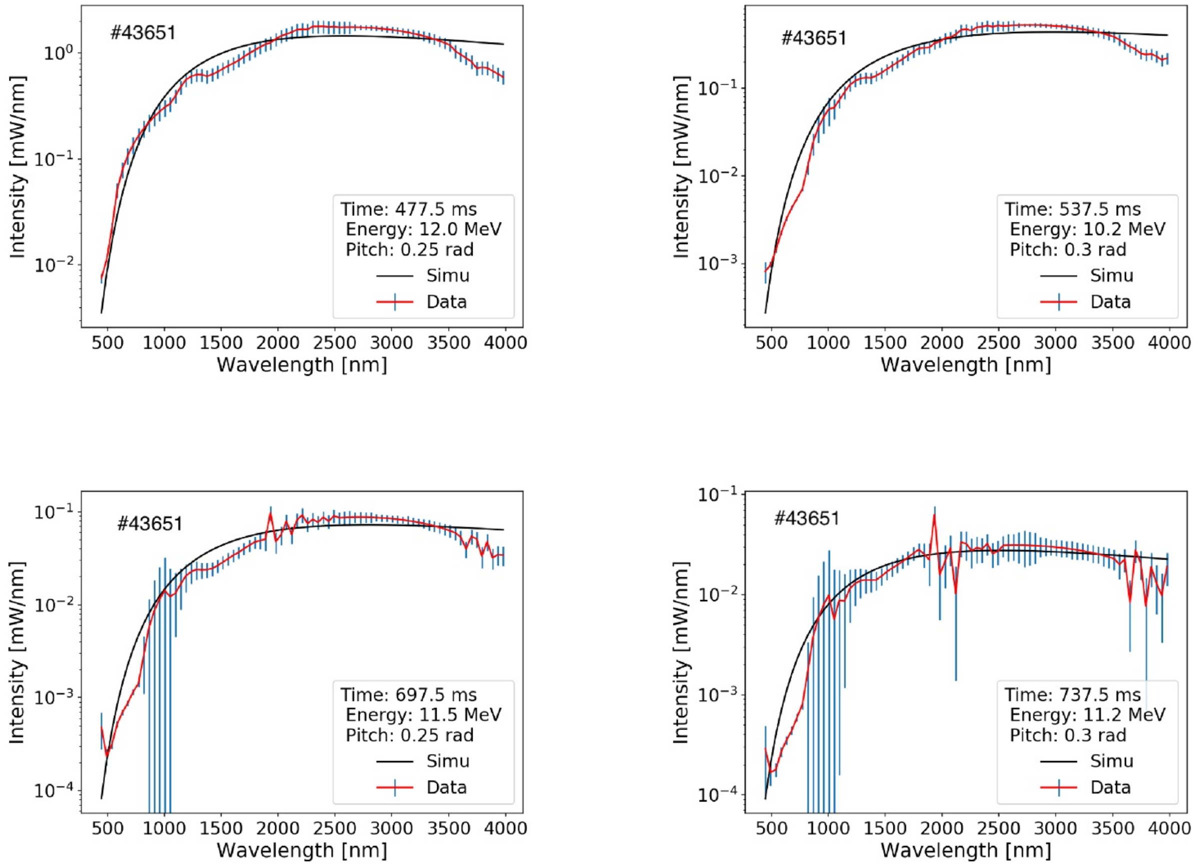

Figure 8. Synchrotron spectra: measured (red line) and simulated best fit (black line) for discharge #43651. Error bars include calibration and counting statistics (square root of the counts).

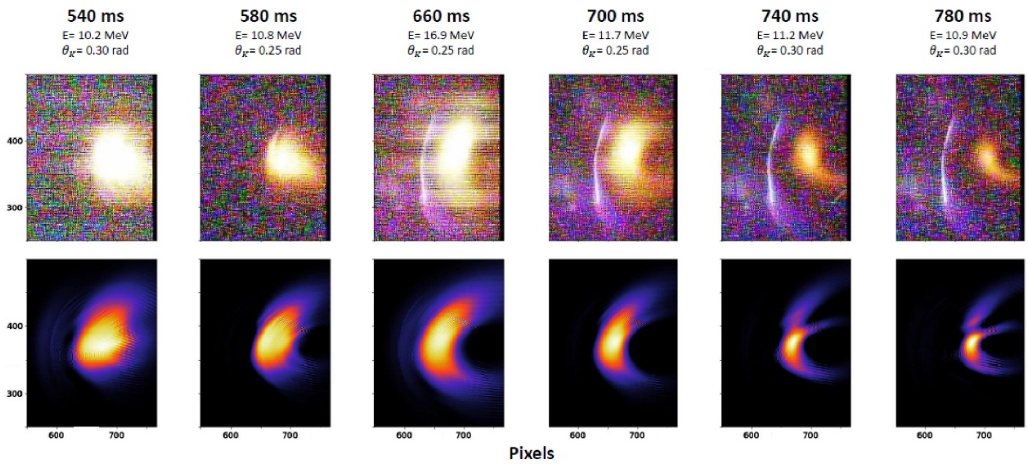

Figure 9. Synchrotron images: measured (top) and simulated image best fit (bottom) for discharge #43651. Note that the simulations have been carried out using the exponential pitch angle distribution and the legend displays the θ_K values.

As discussed in relation to equation (10), the product of the distribution function $f(r,p,\theta_p)$ and the Green's function $\hat{I}$ attains a maximum at the pitch angle value which we denote by θ_K, as shown in figure 13. Around this θ_K, the detected radiation rapidly drops off, and so most of the radiation in the measurement comes from particles with pitch angles in the vicinity of θ_K. This fact allows us to approximate the distribution function even further as a delta function, or mono-pitch distribution, in order to quickly converge on the appropriate value of θ_K. While this approximation works well to reproduce spectra, it is not sufficient to quantitatively reproduce camera images. This is illustrated in figure 11, which shows that using a simple mono-pitch distribution with a Gaussian radial profile, or an exponential pitch distribution with a flat radial profile (see figure 11 center and right, respectively), does not enable a good reconstruction of the experimental image,

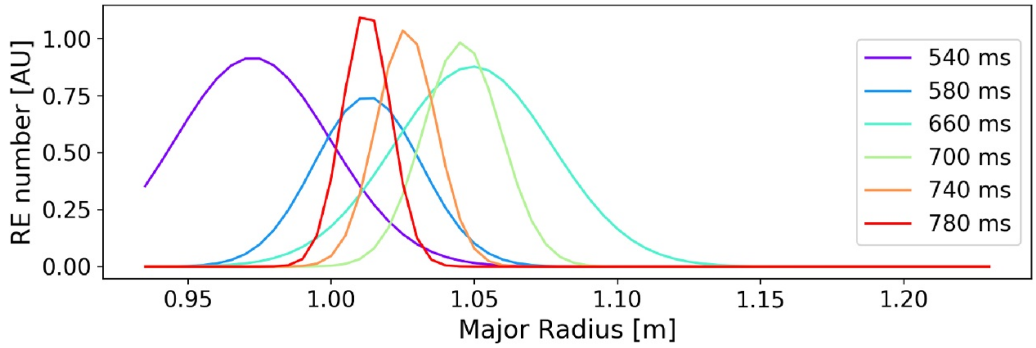

Figure 10. RE radial profiles determined as explained in section 5 for discharge #43651.

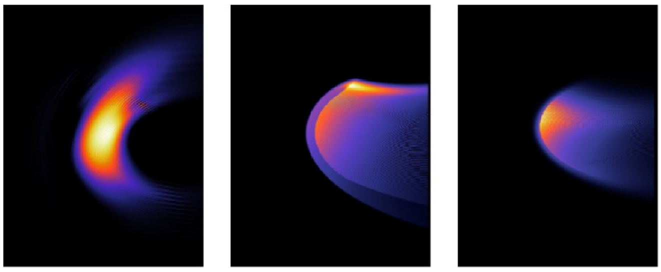

Figure 11. Image reconstruction at 700 ms (discharge #43651) using: exponential pitch distribution and Gaussian radial profile as in figure 9 (left), mono-pitch distribution with Gaussian radial profile as in figure 9 (center) and exponential pitch distribution with flat radial profile (right). In all cases the momentum distribution is a delta function.

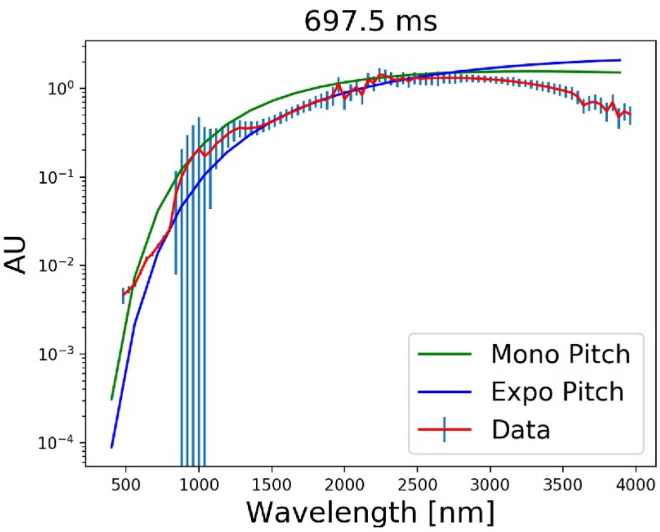

Figure 12. Spectrum calculated at 697.5 ms (discharge #43651) using mono pitch distribution and exponential pitch distribution.

while the combination of exponential pitch angle distribution and Gaussian radial profile is needed (see figure 11 left). On the other hand, the approximation of using a mono-pitch distribution in the initial phase of the analysis (to determine the p^* values) is justified since the effect of the choice of pitch distribution on the calculated spectrum is irrelevant (see figure 12).

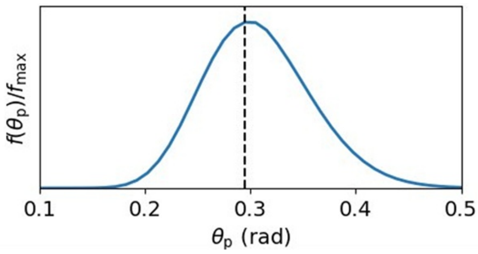

Figure 13. Pitch angle distribution profile: the choice of the parameter K is made by centering the peak of the distribution in the θ_K value selected.

6. Runaway electron dynamics in post-disruption phase

The RE energy, pitch angle, number and radial position estimated for the discharges #43540 and #43651 based on the results of the previous analysis (section 5) are shown in figure 14(panels 2–5) together with the plasma current (panel 1) and loop voltage (panel 6).

The second panel shows the RE energy (green bars) determined in those cases in which no experimental images are present, by setting θ_K in the range 0.25–0.30 rad. The energy estimates at times for which experimental images are available are represented by the black dots. The energy panel also includes, shown as grey area, the energy values obtained from simulations performed with a test particle model (TPM) [4, 35]. These TPM simulations are performed for time intervals right after the formation of the plasma, when the synchrotron radiation emission is still too low to enable spectral or imaging measurements, and use plasma parameter values from experimental data (V_{loop}, line averaged density). The electron energy range is estimated by carrying out the simulations for different values of the inductance L_{int}, which determines the electric field seen by the electrons during the I_p ramp-up and depends on the plasma current profile shape. In particular, the grey area represents energy values obtained by the TPM by varying L_{int} in the range $L_{int} = 0$ (upper values in energy) and $L_{int} = \mu_0 R_0$ (lower values in energy), where μ_0 is the vacuum permeability and R_0 the geometric axis of the device. In discharge #43651, the energy before the disruption is initially 10 MeV; it then increases slightly just after the disruption, followed by

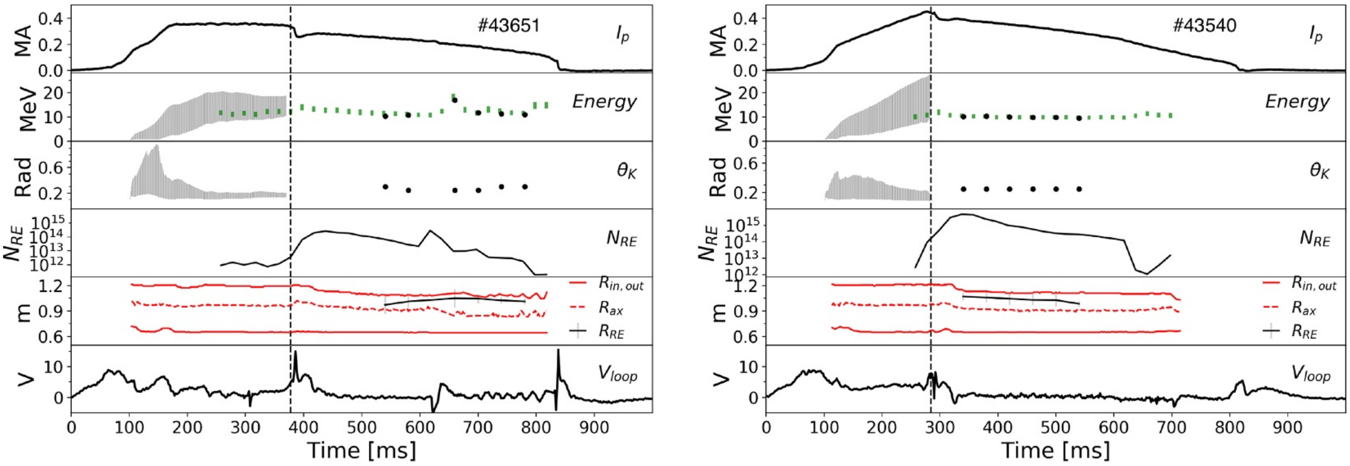

Figure 14. Discharges #43651 (left) and #43540 (right) from top to bottom: I_p; RE energy corresponding to: θ_K values extracted from synchrotron images (black dots), θ_K in the range 0.25–0.30 rad (green bars) and TPM simulations (grey)); θ_K values obtained from synchrotron images (black dots) and from TPM simulations (grey); RE number; major radius of RE radial distribution peak (R_{RE}) with grey bars indicating FWHM of Gaussian radial distribution, plasma inner, outer ($R_{in,out}$) and magnetic axis major radius (R_{ax}); V_{loop}. The dashed vertical line indicates the disruption time.

a gradual decrease until the V_{loop} spike, at $t = 622$ ms, when it reaches 17 MeV. In discharge #43540 the RE energy after an initial rise levels off at 10 MeV, and this value is maintained also after the disruption. There is a good match between the energy values measured by the synchrotron diagnostic and those determined by the TPM in the time interval where they can be compared, namely in the pre-disruption phase.

The third panel of figure 14 shows the RE pitch angle θ_K values. Again, TPM simulation are shown as grey area before the disruption time, while the values determined using the procedure explained in (section 5) are represented by black dots: these data are available only when experimental images are present and therefore no overlap with the TPM simulated data is possible in this case. It is found that higher values of pitch angle are found in this post-disruption phase experiment than during the plasma current ramp-up and flat-top of ohmic discharges in previous experiments: values up to 0.3 rad are found here against prevoious values up to 0.15 rad [5, 6]. Note, however, that the energy and pitch angle values depend on the variability among the different discharges and discharge phases of that plasma parameters [6] affecting the accelerating field (V_{loop}), the collision losses (n_e), the synchrotron losses (B_T) and the pitch angle scattering (Z_{eff}).

The fourth panel of figure 14 shows the number of RE (N_{RE}) determined from the comparison between experimental and simulated spectra (see (section 5) equation (12)). In both discharges, there is a very large increase of N_{RE} in correspondence with the disruption (about two orders of magnitude) followed by a slow decrease. This analysis, therefore, enables us to clarify that the signal increase observed in the neutron, gamma, and synchrotron time traces after the disruption is not related to an increase in the RE energy, but instead to a large variation of the RE number. The RE energy, on the contrary, has just a slight variation. A possible explanation for this is that a significant hot-tail population of electrons could be generated in the disruption, as has been seen in other devices of similar size, e.g. ASDEX Upgrade [21]. This hot-tail population would initially have relatively low energies, but would quickly be accelerated to multi-MeV energies in the current quench. In fact, a time integration of V_{loop} shows that electrons could gain up to 14 MeV energy in #43651, and 11 MeV in #43540, which is close to the measured pre-disruption RE energy. The pre-disruption RE, from which we measure synchrotron radiation before the disruption, would also increase their energies by this amount in the current quench. However, since the pre-disruption RE are much fewer than the hot-tail electrons generated in the disruption, their radiation will be drowned out by that of the hot-tail electrons, which attain approximately the same energies as the pre-disruption RE.

An interesting and different situation, in which both an increase of RE energy and N_{RE} occur, is represented by the transient event at 600 ms (related to a kinetic instability [36]) in discharge #43651. The V_{loop} spike at this time produces an increase of N_{RE} (more than one order of magnitude) followed soon after by a significant increase also of the RE energy (from $\sim$ 10 MeV to $\sim$ 17 MeV).

The fifth panel provides the time traces of the plasma inner, outer ($R_{in,out}$) and magnetic axis major radius (R_{ax}) together with the time trace of the major radius of the center of the RE radial profiles (R_{RE}) as shown in figure 10. It is also worthwhile to note that the transition from a circular to a crescent shape of the synchrotron pattern observed in the experiment is caused by the redistribution of the RE density towards the outer region of the plasma. In particular, compare the images at the time slices 540 ms and 660 ms in (figure 9) and the corresponding RE density profiles in figure 10): the particles on the HFS collectively emit relatively more radiation than those on the LFS, yielding a crescent pattern at 660 ms and beyond.

This is in agreement with what already explained and observed in [21].

7. Conclusion

This work has investigated the behavior of runaway electrons in the post-disruption phase of FTU discharges through the comparison between experimental synchrotron emission spectra (range 450–4000 nm) and visible images and their synthetic counterparts obtained with synthetic diagnostic (SOFT code) simulations. Assuming a given parametrization of the RE distribution function, the RE number, radial profile, energy and pitch angle have been determined from the start-up to the post-disruption phase of runaway discharges, thus providing a comprehensive view of the evolution of RE in a tokamak plasma. The main finding is that the RE number is found to increase by about two orders of magnitude after the disruption, while, in contrast to this, in practice the RE energy and pitch angle maintain after the disruption the same values they had before the disruption. A possible explanation for this is that a significant population of hot-tail electrons is generated in the disruption, and accelerated to the same energies as the pre-disruption RE. The RE maximum energy and pitch angle inferred experimentally have been compared and found in agreement, in the pre-disruption phase, with the results of simulations based on a runaway electron test particle model, thus providing a contribution to the validation the runaway models used to make predictions about runaway generation and dynamics in ITER.

Data availability statement

All data that support the findings of this study are included within the article (and any supplementary files).

Acknowledgments

The authors would like to thank: A Sibio and B Tilia for the help in the diagnostic set-up; S Palomba, M Scisció, F Bombarda, D Liuzza for the diagnostics check during the experiments; O Tudisco for the interferometer data processing; P Buratti, D Carnevale, C Castaldo, S Ceccuzzi, M Iafrati, G Ramogida for the FTU program operations; A Buscarino, L Fortuna, T Fülöp and G Mazzitelli for the support on the project. This work has been carried out within the framework of the EUROfusion Consortium, funded by the European Union via the Euratom Research and Training Programme (Grant Agreement No 101052200 EUROfusion). Views and opinions expressed are however those of the author(s) only and do not necessarily reflect those of the European Union or the European Commission. Neither the European Union nor the European Commission can be held responsible for them. Part of this work was done under financial support from Projects ENE2015-66444-R (MINECO/FEDER, UE) and PID2019-110734RB-I00 (AEI, Spain).

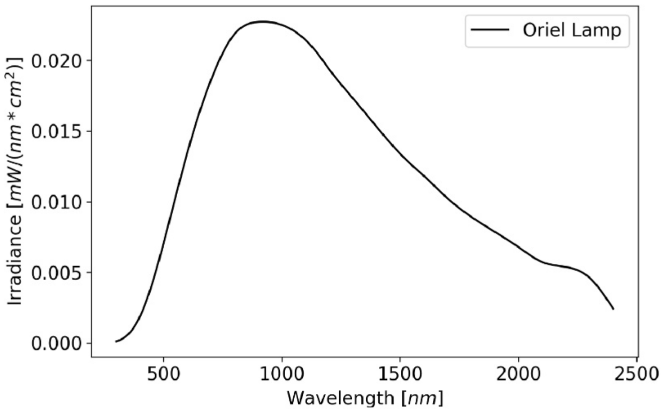

Figure 15. Nominal power spectra emitted by the Oriel source at 50 cm distance (calibration provided by the company).

Appendix. Calibration of spectrometers

This appendix explains how the spectral response of the REIS spectrometer system was calibrated in ENEA laboratories. For the calibration, two different light sources were used. The first one is a quartz halogen tungsten lamp of 1000 W made by Oriel, absolutely calibrated in irradiance (W nm^{-1} cm^{2}) in the range 400 nm–2500 nm; the second one a ThorLab lamp covering a wider range spectrum (400–5500 nm), but not absolutely calibrated. The power spectra are shown in figures 15 and 16.

The calibration consists in comparing the nominal lamp power spectrum with the signal measured by the spectrometers. The ThorLab source is used for obtaining the relative response of all the spectrometers, due to its spectral range, while the Oriel source is used for fixing the power units (mW/(nm x count)). The background is subtracted off the spectrometer signal and the calibration curve is computed as the ratio of nominal lamp radiance to the raw spectrometer signal:

$$\mathrm{Calib} = \frac{\text{Lamp Nominal Power}}{\text{Detector signal}}. \qquad (13)$$

The Oriel Lamp calibration was performed at a distance of 50 cm. The ThorLab lamp was instead placed close to the REIS head in order to maximize the signal. The two calibrations curves were then compared in order to fix the units of the ThorLab one. By calculating the ratio of the two calibrated signals, the correction factor $D = C_{\mathrm{or}}/C_{\mathrm{th}}$ for the absolute calibration of the ThorLab lamp in W nm^{-1} is found in each spectrometer range. Due to the limitation of the Oriel lamp wavelength range it was supposed that $D_{\mathrm{NIR}} = D_{\mathrm{MIR}}$. The scale factors were found using the minimization of the sum of the square uncertainties, $E(D)$.

$$E(D) = \sum_{\lambda} \left(C_{\mathrm{or}}^{\lambda} - D \cdot C_{\mathrm{th}}^{\lambda}\right)^2 \qquad (14)$$

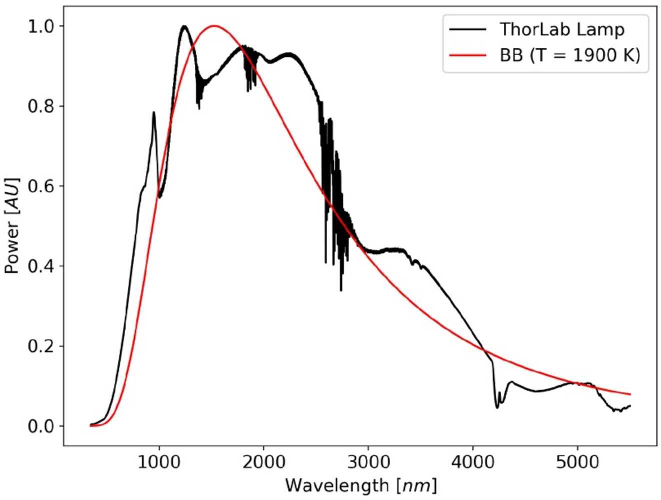

Figure 16. Normalized power spectra emitted by the ThorLab source compared to black body emission at 1900 K.

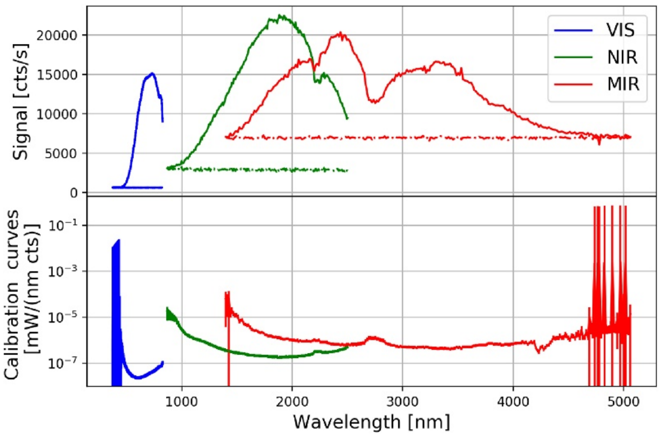

Figure 17. Top panel: raw signal (solid lines) and background (dashed lines). Bottom panel: calibration curves.

We then find *D*:

$$D = \frac{\sum_{\lambda} C_{\rm or}^{\lambda} \cdot C_{\rm th}^{\lambda}}{\sum_{\lambda} {C_{\rm th}^{\lambda}}^2} \tag{15}$$

The final calibration curves are presented in figure 17.

Figure 18 shows the different sources of uncertainty. Since the ThorLab lamp was not calibrated, we assumed a conservative uncertainty of 15% on the expected intensity shape (red line). The other sources considered are the square root of the signal counts (blue line) and the uncertainty on the correction factor *D* (yellow line).

As it can be seen from the bottom panel of figure 18 the uncertainty on the lamp dominates the total uncertainty. Hence, the calibration can be improved using an absolutely calibrated source in the whole wavelength range (this is foreseen in the next upgrade of the system).

The range of wavelengths chosen for the analysis for the spectrometers has been limited to those wavelength intervals where the total uncertainty is below 20%. The ranges are the following: VIS: (490–820) nm, NIR: (960–2450) nm, MIR:

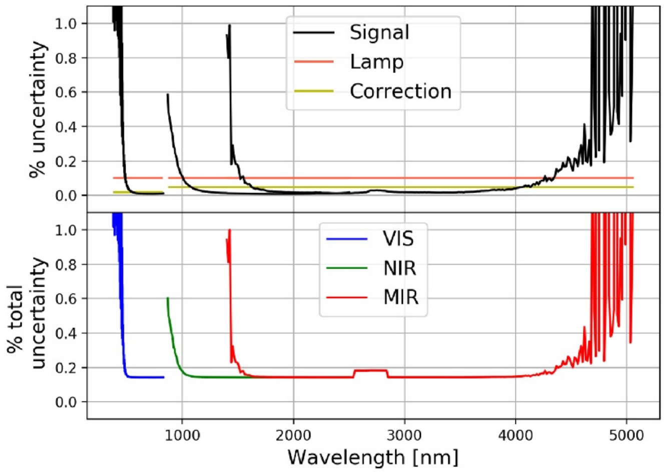

Figure 18. Top panel: the total relative uncertainty on the calibration. Bottom panel: different uncertainty components.

(1560–4400) nm. Therefore the overall effective range adopted for the data analysis is (450–4000) nm.

ORCID iDs

G Ghillardi https://orcid.org/0000-0002-0814-7803
B Esposito https://orcid.org/0000-0002-0005-5680
M Hoppe https://orcid.org/0000-0003-3994-8977
G Pucella https://orcid.org/0000-0002-9923-2770
J R Martín-Solís https://orcid.org/0000-0003-0458-4405
F Causa https://orcid.org/0000-0003-0508-3100

References

[1] Hender T C *et al* 2007 Chapter 3: MHD stability, operational limits and disruptions *Nucl. Fusion* **47** S128–202
[2] Breizman B N, Aleynikov P, Hollmann E M and Lehnen M 2019 Physics of runaway electrons in tokamaks *Nucl. Fusion* **59** 083001
[3] Esposito B *et al* 2003 Dynamics of high energy runaway electrons in the Frascati Tokamak Upgrade *Phys. Plasmas* **10** 2350–60
[4] Martín-Solís J R, Esposito B, Sánchez R and Alvarez J D 1999 Energy limits on runaway electrons in tokamak plasmas *Phys. Plasmas* **6** 238–52
[5] Esposito B E *et al* 2017 Runaway electron generation and control *Plasma Phys. Control. Fusion* **59** 014044
[6] Popovic Z *et al* 2016 On the measurement of the threshold electric field for runaway electron generation in the Frascati Tokamak Upgrade *Phys. Plasmas* **23** 122501
[7] Causa F *et al* 2015 Cherenkov emission provides detailed picture of non-thermal electron dynamics in the presence of magnetic islands *Nucl. Fusion* **55** 123021
[8] Martín-Solís J, Sanchez R and Esposito B 2010 Experimental observation of increased threshold electric field for runaway generation due to synchrotron radiation losses in the FTU tokamak *Phys. Rev. Lett.* **105** 185002
[9] Carnevale D *et al* 2021 Results on quiescent and post-disruption runaway electrons studies at Frascati Tokamak Upgrade: RE mitigation via solid deuterium pellets and anomalous doppler instability *Nucl. Fusion* **61** 116050

[10] Finken K H *et al* 1990 Observation of infrared synchrotron radiation from tokamak runaway electrons in textor *Nucl. Fusion* **30** 859
[11] Jaspers R *et al* 2001 A synchrotron radiation diagnostic to observe relativistic runaway electrons in a tokamak plasma *Rev. Sci. Instrum.* **72** 466
[12] Chen Z Y *et al* 2006 Measurement of the runaway electrons in the HT-7 tokamak *Rev. Sci. Instrum.* **77** 013502
[13] Zhou R *et al* 2014 Synchrotron radiation spectra and synchrotron radiation spot shape of runaway electrons in experimental advanced superconducting tokamak *Phys. Plasmas* **21** 063302
[14] Zhang Y *et al* 2021 Analysing the distribution of runaway electrons in the east tokamak based on soft *Fusion Eng. Des.* **173** 112924
[15] Cheon M *et al* 2018 Observation of thermal quench induced by runaway electrons in magnetic perturbation *Nucl. Fusion* **58** 046020
[16] Tinguely R A *et al* 2018 Spatiotemporal evolution of runaway electrons from synchrotron images in alcator c-mod *Plasma Phys. Control. Fusion* **60** 124001
[17] Hoppe M, Embréus O, Tinguely R A, Granetz R S, Stahl A and Fülöp T 2018 Soft: a synthetic synchrotron diagnostic for runaway electrons *Nucl. Fusion* **58** 026032
[18] Hoppe M *et al* 2021 Runaway electron synchrotron radiation in a vertically translated plasma *Nucl. Fusion* **60** 094002
[19] Wijkamp T *et al* 2021 Tomographic reconstruction of the runaway distribution function in tcv using multispectral synchrotron images *Nucl. Fusion* **61** 046044
[20] Reux C *et al* 2021 Demonstration of safe termination of megaampere relativistic electron beams in tokamaks *Phys. Rev. Lett.* **126** 175001
[21] Hoppe M *et al* 2021 Spatiotemporal analysis of the runaway distribution function from synchrotron images in an asdex upgrade disruption *J. Plasma Phys.* **87** 1 2021
[22] Yu J *et al* 2013 Visible imaging and spectroscopy of disruption runaway electrons in DIII-D *Phys. Plasmas* **20** 042113
[23] Tinguel R A *et al* 2018 Measurements of runaway electron synchrotron spectra at high magnetic fields in Alcator C-Mod *Nucl. Fusion* **58** 076019
[24] Causa F *et al* 2019 Runaway electron imaging spectrometry (REIS) system *Rev. Sci. Instrum.* **90** 073501
[25] Pucella G *et al* 2022 Overview of the FTU results *Nucl. Fusion* **62** 042004
[26] Martín-Solís J, Loarte A, Hollmann E, Esposito B and Riccardo V 2014 Inter-machine comparison of the termination phase and energy conversion in tokamak disruptions with runaway current plateau formation and implications for ITER *Nucl. Fusion* **54** 083027
[27] De Angelis R and Di Matteo L 2010 Observations and analysis of FTU plasmas by video cameras *Nucl. Instrum. Meth. Phys. Res. A* **623** 815–7
[28] Itseez 2015 Open source computer vision library (available at: https://github.com/itseez/opencv/)
[29] Tomes M 2024 Forward and backward modelling of spectroscopic diagnostics in fusion plasmas, phd thesis, faculty of mathematics and physics, charles university, prague (available at: http://hdl.handle.net/20.500.11956/188741/)
[30] Schwinger J S 1949 On the classical radiation of accelerated electrons *Phys. Rev.* **75** 1912
[31] Hoppe M, Embréus O, Paz-Soldan C, Moyer R A and Fülöp T 2018 Interpretation of runaway electron synchrotron and bremsstrahlung images *Nucl. Fusion* **58** 082001
[32] Connor J and Hastie R 1975 Relativistic limitations on runaway electrons *Nucl. Fusion* **15** 415
[33] Breizman B N 2014 Marginal stability model for the decay of runaway electron current *Nucl. Fusion* **54** 072002
[34] Aleynikov P and Breizman B N 2015 Theory of two threshold fields for relativistic runaway electrons *Phys. Rev. Lett.* **114** 155001
[35] Martín-Solís J R, Esposito B, Sánchez R, Poli F M and Panaccione L 2006 Enhanced production of runaway electrons during a disruptive termination of discharges heated with lower hybrid power in the Frascati Tokamak Upgrade *Phys. Rev. Lett.* **97** 165002
[36] Buratti P *et al* 2021 Fast dynamics of radiofrequency emission in FTU plasmas with runaway electrons *Plasma Phys. Control. Fusion* **63** 095007